Drag Predictions for Projectiles and Finned Bodies in Incompressible Flow

Walter P. Wolfe* and William L. Oberkampf†
Sandia National Laboratories, Albuquerque, New Mexico

A design method is presented for calculating the flowfield and drag of bodies of revolution, with and without aerodynamic surfaces, at zero angle of attack in incompressible flow. The body pressure distribution, viscous shear stress, and boundary-layer separation point are calculated by a combination of a potential-flow method and boundary-layer techniques. The potential solution is obtained by modeling the body with an axial distribution of source/sink elements whose strengths vary linearly along their length. Both the laminar and turbulent boundary-layer solutions use momentum integral techniques which have been modified to account for the effects of surface roughness. An existing technique for estimating the location of transition was also modified to include surface roughness. Empirical correlations are developed to estimate the base pressure coefficient for a wide variety of geometries. Body surface pressure distributions and drag predictions are compared with experimental data for artillery projectiles, conical bodies, bombs, and missiles. Very good agreement between the present method and experiment is obtained.

Nomenclature

A_{ref} = reference area = $\pi d^2/4$
C_D = drag coefficient = $D/q_\infty A_{\text{ref}}$
C_p = pressure coefficient = $(P-P_\infty)/q_\infty$
D = drag
d = maximum body diameter
H = shape factor = δ^*/θ
k_s = equivalent sand-grain roughness
L = body length
M = Mach number
m = boundary-layer transition parameter
P = pressure
q = dynamic pressure = $\frac{1}{2}\rho U^2$
Re = Reynolds number
r = local body radius
S = reference area for base pressure correlation
s = surface length
U = velocity
x = axial coordinate
β = body slope at base
δ = boundary-layer thickness
δ^* = boundary-layer displacement thickness
η = boundary-layer transition parameter
Θ = boundary-layer momentum thickness
μ = absolute viscosity
ν = kinematic viscosity
ρ = density
Ψ = Strokes stream function

Superscripts and Subscripts

$(\ )_{as}$ = aerodynamic surfaces
$(\ )_b$ = base
$(\ )_{\text{bnd}}$ = firing band
$(\ )_c$ = cylinder
$(\ )_{\text{crit}}$ = critical value
$(\ )_i$ = value at point of instability
$(\ )_\ell$ = laminar boundary layer
$(\ )_{\text{lug}}$ = lugs
$(\ )_p$ = pressure
$(\ )_{\text{ref}}$ = reference value
$(\ )_s$ = separation
$(\ )_t$ = turbulent boundary layer
$(\ )_{tr}$ = bounday-layer transition
$(\ )'$ = (d/ds)
$(\ )_\infty$ = freestream value

Introduction

IN the preliminary stages of flight vehicle design, it is important that the designer have a means of obtaining reasonably accurate estimates of the vehicle's aerodynamic characteristics. Typically, the most important aerodynamic performance characteristics are drag and/or lift-to-drag ratio. Other characteristics important in aerodynamic optimization are the individual components of drag and the boundary-layer separation point. This work describes a design method for obtaining the flowfield and drag components quickly and simply for bodies of revolution, with or without aerodynamic surfaces, at zero angle of attack in incompressible flow. Any aerodynamic surfaces, either control surfaces, lifting surfaces, or stabilizing fins, must also be at zero angle of attack.

The approach taken here is the classical coupling of the potential flow solution with the boundary-layer solution. The potential flow solution uses an axial distribution of source/sink elements whose strengths vary linearly over the length of each element. Both the laminar and turbulent boundary-layer solutions use momentum integral techniques which have been modified to account for the effects of surface roughness. An existing technique, also modified to include surface roughness, is used to estimate boundary-layer transition. Boundary-layer separation, if it occurs, is modeled by modifying the potential flow solution in an iterative manner. Empirical correlations are developed to estimate the base pressure coefficient for a wide variety of geometries.

A computer program, SANDRAG, which is available for U.S. government contract applications, was written to implement the present analytical method. This code was designed to be easy to use in a design environment. To verify that the code gives accurate predictions, the current work makes com-

---

Presented as Paper 85-0104 at the AIAA 23rd Aerospace Sciences Meeting, Reno, NV, Jan. 14–17, 1985; received March 14, 1985; revision received Dec. 27, 1985.

*Member of Technical Staff, Aerodynamics Department. Senior Member AIAA.

†Member of Technical Staff, Aerodynamics Department. Associate Fellow AIAA.

parisons with experimentally measured pressure distributions and total vehicle drag of several body geometries.

Potential Flow Solution

One of the most general methods of calculating the potential solution about arbitrary bodies is the surface singularity method, such as that described by Hess and Smith.[1] This class of methods can treat almost any geometry, but they are rather complicated to use and require relatively large amounts of computer time and memory. A much simpler, but more restrictive, class of methods for axisymmetric bodies are the line singularity methods. The simplest method in this class, known as von Karman's method, uses an axial distribution of constant strength source/sink elements. Although von Karman's method works well for certain shapes, such as Rankine bodies, Oberkampf and Watson[2] have shown that the equations are ill-conditioned for certain body geometries, giving results which are not always reliable. Precision on the order of 29 decimal digits (double precision on CDC-type machines) is needed even for simpler shapes.

A more general method of obtaining the potential solution was originally developed by Zedan and Dalton[3] who used an axial distribution of source/sink elements; each source strength varies linearly over the length of the element. While this method is superior to von Karman's method, i.e., it gives more accurate results for a larger variety of body shapes, it retains the simplicity of the von Karman method and requires much less computer time and memory than the surface singularity methods. Zedan and Dalton concluded that only 8-digit precision was required to obtain accurate results. The equations presented by Zedan and Dalton apply only to closed bodies, i.e., the surface streamline returns to the axis at the aft end of the body. In previous work by the present authors,[4] the equations were extended to cover open bodies, i.e., bodies which have a nonzero base diameter or whose boundary layer separates from the surface.

Zedan and Dalton[5] and Christopher and Shaw[6] have investigated the axial source distribution technique using higher-order polynomial distributions of source strength along the body axis. For their test cases, Zedan and Dalton concluded that the linear strength variation gave good results for simple bodies with a rounded nose and tail. A combination of linear and parabolic variations worked well for bodies with inflection points and a sharp nose or tail. Christopher and Shaw concluded that a smaller number of higher-order polynominal distributions (up to degree 10) provided adequate solutions for bodies which had small discontinuities in surface curvature. Considerable insight, however, is required to determine the number and degree of the polynomials and the proper distribution of the surface control points.

In the method used in the present work, the potential solution is obtained by modeling the body of revolution by an axial distribution of source/sink elements. The strength of each element is allowed to vary linearly over its length. The strengths of adjacent elements are equal at their juncture. For a body with N source elements, N linear algebraic equations with $N+1$ unknowns are obtained by requiring that an arbitrary streamline pass through N surface points on the body. The remaining equation used to close the system depends upon an additional constraint chosen for the body surface boundary condition.

Description of the Method

The potential flow equations used in the present work are identical to those derived previously by Wolfe and Oberkampf.[4] To conserve space, they will not be repeated here. The only change in the potential solution from that described in Ref. 4 is the manner of distribution of the surface control points. The new procedure for this distribution gives a more accurate definition of the body.

In the present work, it was found that the quality of the potential flow solution was dependent upon the location of the source/sink elements and the surface control points for certain types of bodies. By quality of the solution, it is meant that even though the body surface streamline ($\Psi = 0$) passes through all of the control points, the streamline does not represent the actual surface. For example, the streamline may undulate between the control points. Numerical experiments were conducted to determine the best locations for both the control points and the source elements. It was found that the surface control points must be centered over the corresponding source elements. Failure to do so can result in an ill-conditioned set of equations which cannot always be solved. For bodies with discontinuous body slopes, e.g., cone-cylinders, it was found that the best results were obtained if the control points were positioned so that there was a control point at each of the junctures of the body components. Distributing the control points in this manner gave a good definition of body slope discontinuities and, therefore, a good prediction of the pressure spikes which occur at these discontinuities.

The computer program, SANDRAG, is written such that commonly used body components, for example, tangent ogives and conical sections, are options the user can pick during input. One can also program special body components or input tabular body points. The program-supplied-component options automatically satisfy the recommended distribution of control points, whereas user-supplied components must be input such that they satisfy the above mentioned criteria. Details of the theoretical development and computer program are given in Refs. 7 and 8.

Boundary-Layer Solution

Once the flowfield has been obtained from the potential solution, the boundary-layer calculations can be performed. In the present work, the boundary-layer solution is obtained using momentum integral techniques. The boundary-layer calculations are made independently for both the body of revolution and aerodynamic surfaces. Both boundary-layer solutions account for the effects of pressure gradient and surface roughness. Only the pressure gradient due to the body of revolution is considered. The effects of surface roughness on the development of the boundary layer are dependent upon the type of roughness present. Only the effects of distributed, three-dimensional roughness, e.g., sand, have been considered in the present work.

Laminar Boundary Layer

The solution for the laminar portion of the boundary layer is obtained from Thwaites' one parameter solution of the momentum integral equation.[9,10] For steady flow over an axisymmetric body with impermeable walls, it is assumed that the boundary-layer thickness, δ, satisfies the condition $\delta \ll r$. The momentum integral equation can be integrated to give

$$\Theta^2 = \frac{0.45\mu}{r^2 U^6 \rho} \int_0^s r^2 U^5 \mathrm{d}s \tag{1}$$

where Θ is the momentum thickness and U is the surface velocity from the potential solution. Once the momentum thickness is obtained from Eq. (1), the remaining laminar boundary-layer parameters are obtained from a tabulated correlation among the parameters.[10]

The laminar boundary layer on the aerodynamic surfaces is also calculated using Thwaites' one parameter method. The aerodynamic surfaces are assumed to be at zero lift and their boundary layer is only influenced by the pressure gradient of the body of revolution. The equation for Θ on the aerodynamic surfaces is identical to Eq. (1) except for the elimination of the r^2 terms.

An extensive literature search failed to document any quantified effects of surface roughness on laminar boundary-layer characteristics. A study into the effects of surface roughness

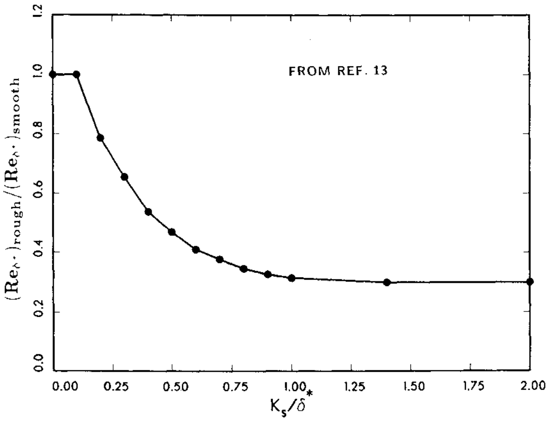

Fig. 1 Effects of surface roughness on boundary-layer transition.

on transition conducted by Casarella and Niedzwecki[11] concluded that there were no significant effects of roughness on the displacement thickness of a laminar boundary layer. For the present method, it is assumed that the only effect of surface roughness on the laminar boundary layer is to hasten transition.

Boundary-Layer Transition

The point of transition is calculated in the present work by the approximate method of Schlichting and Ulrich.[10,12] It is assumed that the method applies equally well to the flat aerodynamic surfaces and the body of revolution. First, the point of instability, s_i, where the unsteady Tollmien-Schlichting waves first appear, is determined. This determination is made using the local Reynolds number based on displacement thickness, Re_{δ^*}. At each step in the laminar calculation, the local values of Re_{δ^*}, and the parameter η, defined as

$$\eta = 2m/(1+m) \tag{2}$$

where

$$m = sU'/U$$

are calculated. This local η is used to determine the local value of $Re_{\delta^*,\mathrm{crit}}$ from a correlation of stability parameters for Falkner-Skan profiles.[10] The flow is unstable when $Re_{\delta^*} \geq Re_{\delta^*,\mathrm{crit}}$. Once s_i is known, the transition point, s_{tr}, is determined by examining Re_Θ. A transition value of Re_Θ is determined from

$$Re_\Theta(tr) = Re_\theta(s_i) + 450 + 400\exp(60\lambda_m) \tag{3}$$

where

$$\lambda_m = \frac{1}{s_{tr} - s_i}\int_{s_i}^{s_{tr}} \lambda(s)\mathrm{d}s$$

When $Re_\Theta(s) \geq Re_\Theta(tr)$, the flow has transitioned.

Kluck[13] presented experimental data for the effect of distributed roughness on transition. He correlated displacement-thickness Reynolds number Re_{δ^*} at transition with the ratio of roughness height to displacement thickness k_s/δ^*. The equivalent sand-grain roughness, k_s, is the average height, peak to valley, of the grains of uniform, distributed sand. Figure 1 shows a functional approximation of Kluck's experimental data used in the present method. This figure shows that as the surface roughness increases, the transition value of Re_{δ^*} is reduced from the value for a smooth surface. In implementing the effects of surface roughness on boundary-layer transition, it is assumed that the data shown in Fig. 1 apply to the reduction in both critical displacement thickness Reynolds number and transition momentum thickness Reynolds number.

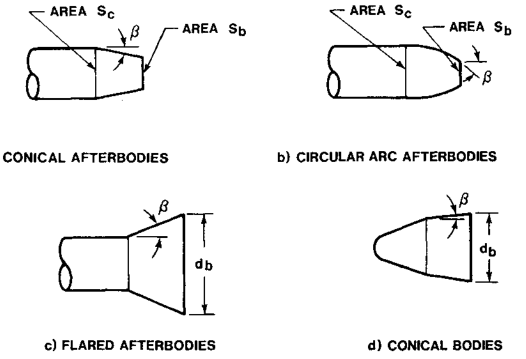

a) CONICAL AFTERBODIES

b) CIRCULAR ARC AFTERBODIES

c) FLARED AFTERBODIES

d) CONICAL BODIES

Fig. 2 Geometric categories for base pressure drag calculation.

Turbulent Boundary Layer

Once the flow has transitioned, the turbulent boundary-layer solution is initiated. The method chosen in the present work is a modification of White's Karman-type method[10] for nonequilibrium pressure-gradient flows. The method has been modified to account for the effects of surface roughness. For turbulent flow, small roughness elements at the surface will break up the thin viscous layer and cause strong changes in the velocity profile. As with the laminar boundary-layer equations, the method assumes that $\delta \ll r$. In terms of a Reynolds number based on radius, White states that the method gives accurate results as long as $rU/\nu > 10^3$.

The complete set of equations for all of the variables in the turbulent boundary-layer solution are given in Refs. 7 and 8. The set of equations is solved simultaneously by iteration at each step along the body and aerodynamic surfaces where a turbulent boundary layer exists. The solution begins at the point of transition and proceeds to each succeeding body station using a simple Euler integration method for the differential equations in the set. The solution to these equations is started with the value of Θ obtained from the laminar solution and an initial value of the shape factor H of 1.4.

The turbulent separation criterion is not as well defined as for the laminar case. Sovran[14] presents a good discussion of the problems encountered when trying to predict turbulent separation. The most commonly used criterion for determining turbulent separation is based on the shape factor H. Although the values quoted in the literature for H at separation range from 1.8 to 4.05,[10,12,14,15] in the present work, it was found that when H exceeded a value of 1.8, the rate of growth of H increased rapidly and the iterative calculation would not converge. Therefore, it was decided that the separation criterion would be that $H > 1.8$. Because of the rapid growth of H as the boundary layer approaches separation, the ambiguity in the exact value at separation results in small differences in the predicted separation point.

Base Pressure Estimate

Body of Revolution

The component of drag due to base pressure can be a significant part of total drag in subsonic flow. The base drag percentage of total drag can vary from 10% for slender boattailed bodies up to a surprising 99% for cones. The base-drag component on bodies of revolution has generally been determined either by indirect or direct means. Indirect determination involves estimating all the other components of drag, measuring the total drag on a number of geometries, and then assuming that the difference is the base drag component. This approach was taken by McCoy[16] in predicting the drag coefficient of projectiles.

The present work takes the direct approach, whereby a correlation of experimentally measured base pressures is included in the drag prediction method. An extensive literature search was conducted in order to obtain base pressure data on a wide variety of geometries and for a large range of Reynolds numbers. Geometries were classified into four categories (Fig. 2): cylindrical centerbodies with conical afterbodies, cylindrical centerbodies with circular arc afterbodies, cylindrical centerbodies with flared afterbodies, and conical bodies. All of these geometries must have the same base pressure when the afterbody length is zero or when the angle β approaches zero.

For conical and circular arc afterbodies, Payne, Hartley, and Taylor[17] have correlated extensive base pressure data from six experimental investigations. These experiments did not use a rear sting mounted model, which can affect the base pressure, and they covered the Mach number range 0.6 to 1.3. The present work uses Payne's correlations for $M_\infty = 0.6$. These data should be equally applicable at lower subsonic Mach numbers, because the critical Mach number of these afterbodies is greater than 0.6.

The correlations use two geometry inputs in order to determine base pressure coefficient

$$C_{P_b} = (P_b - P_\infty)/q_\infty \tag{4}$$

where P_b = base pressure, P_∞ = freestream static pressure, and q_∞ = freestream dynamic pressure. For conical afterbodies (Fig. 2a), the inputs are boattail angle β and base-to-centerbody area ratio S_b/S_c. Table 1 gives the tabular form of the data for conical afterbodies. (Data from Ref. 17 were linearly extrapolated from $S_b/S_c = 0.1$ to $S_b/S_c = 0.0$ for the present method.) For circular arc afterbodies (Fig. 2b), the inputs are boattail angle at the base β and the base-to-centerbody area ratio S_b/S_c. Table 2 gives the tabular form of the data for circular arc afterbodies. Using linear interpolation with Tables 1 and 2 will accurately reproduce Payne's correlations.

For conical bodies, only one experiment could be found which measured base pressure on conical bodies in low-subsonic flow without a rear sting mount. Pepper and Holland[18] measured the base pressure on a sharp cone with a half-angle of 15 deg. Only one similar experiment of base pressure measurement on a flared afterbody could be found. Butsko, Carter, and Herman[19] measured the base pressure on a 10 deg flare afterbody with a centerbody-to-base diameter ratio of 0.665. Since the base pressure is primarily dependent on the angle of the cone or the flare β, one correlation of these data will be used. Note that when $\beta = 0$ deg for a cone or flare, $C_{P_b} = -0.13$. A single function which represents these data is

$$C_{P_b} = -0.13(1 + 3.1\sqrt{\sin\beta}) \tag{5}$$

The data used by Payne, Hartley, and Taylor[17] for conical and circular arc afterbodies were only for turbulent boundary layers. For this case, they conclude that there is no large effect of Reynolds number on C_{P_b}. In the present method the turbulent boundary-layer correlation is also used for a laminar boundary layer on the afterbody. This use, however, is of questionable accuracy.

Pepper and Holland,[18] in their measurements on cones, do not mention if the boundary layer was laminar or turbulent at the base. Using the present method for calculating the boundary layer and estimating transition, one finds that the boundary layer at the base was laminar for their experiment. Butsko, Carter, and Herman[19] state that the boundary layer was turbulent on their flared afterbody. It is believed that C_{P_b} would be less sensitive to the boundary-layer character on these geometries, because the separation point does not depend on Reynolds number, i.e., it is fixed at the edge of the cone or flare. Therefore, the above correlation, Eq. (5), is used for both laminar and turbulent separation on cones and flared afterbodies.

Table 1 Base pressure coefficient for conical afterbodies (from Ref. 17): S_b/S_c

β	1.0	0.9	0.0
0	−0.13	−0.13	−0.13
4	−0.13	−0.085	0.00
8	−0.13	−0.054	0.067
12	−0.13	−0.036	0.108
16	−0.13	−0.013	0.130

Table 2 Base pressure coefficient for circular arc afterbodies (from Ref. 17): S_b/S_c

β	1.0	0.9	0.0
0	−0.13	−0.13	−0.13
8	−0.13	−0.088	0.00
16	−0.13	−0.030	0.0148
24	−0.13	−0.012	0.216
32	−0.13	−0.061	0.193
40	−0.13	−0.107	0.149
48	−0.13	−0.13	0.142

Fins

Aerodynamic surfaces used on missiles or bombs quite often have blunt trailing edges. Although the base area of the surface may be small, the base drag can represent as much as 10% of the total vehicle drag and, therefore, should not be neglected. Only one reference[20] was found which gives any fin base pressure data. These data can be adquately represented by the equation

$$C_{P_f} = -2.2\sqrt{t_b/c} \tag{6}$$

where C_{P_f} = fin base pressure coefficient, t_b = thickness of fin trailing edge, and c = fin chord length at a given spanwise location.

Solution Procedure

The equations described in the previous sections are implemented in the following manner. The potential flow equations are solved using a sufficient number of sources (generally between 20 and 40) in order to define the body geometry. The body surface control points are distributed in such a manner that there is always a control point at each of the junctures of the different body components. This procedure permits better body definition and, therefore, a more accurate potential solution when there are discontinuous slopes at these points. The number of control points assigned to each body component is determined by the ratio of the length of the component to the total body length. Within each component, the axial distances between control points are equal. The first control point of the nose component is located at an axial station equal to one-half of the axial distance between the remainder of the control points for that component.

For open bodies, a control point is located at the aft end of the body and an extra control point is located aft of the body. For open bodies with boattails, the extra control point is located aft of the body at a distance equal to the axial distance between control points of the aft body component. The radial coordinate of this extra control point is located by projecting the body surface aft to the correct axial coordinate. For flared bodies and cones, comparison with experimental pressure distributions indicates that the extra control point should be located aft of the body on a line drawn from the body surface at an angle equal to five-eighths of the flare or cone angle. The axial distance to this extra control point is the same as for a boattailed body.

The nodes, or junctures, of the linear source/sink elements are located on the x-axis, midway between each of the surface control points. Several numerical experiments were conducted in order to determine the relative location of the start and end of the singularity distribution to the beginning and end of the body. It was found that best results were generally obtained when the body and singularity distribution started at the same point. For closed bodies, the singularity distribution also ends at the aft end of the body. For open bodies, the final source/sink element extends aft of the body to a point midway between the final two control points. Numerical experimentation has shown that this relative distribution between control points and singularity element gives the best conditioned set of equations for the potential solution. The condition of the coefficient matrix is generally improved by decreasing the number of control points.

The surface velocity and velocity gradient are calculated directly from the potential solution at the control points. A double quadratic interpolation is used to determine the radial coordinate of the surface and the surface velocity at intermediate surface points. Once the velocity and velocity-gradient distributions are obtained from the potential solution, they are used to solve the boundary-layer equations. While the potential solution is solved for typically 20 to 40 points, the boundary-layer equations are evaluated at a larger number of body points; normally 200. For geometries with continuous body slopes, computation of the boundary layer and transition from laminar to turbulent flow is straight forward. However, for bodies with a discontinuous body slope, e.g., cone-cylinders, the computation is altered in order to emulate physically observed phenomena. It is well-known experimentally that at a discontinuous body slope, the laminar boundary layer usually separates, transitions, and reattaches as a turbulent boundary layer. In this solution procedure, the length of the separation bubble is approximated by attempting to calculate the turbulent boundary-layer solution after laminar separation. For the first few axial steps after laminar separation, the turbulent boundary-layer calculations may exceed the turbulent separation criterion. It is assumed that the boundary layer has reattached at the first step at which the iterative solution of the turbulent boundary-layer equations converges.

A total of three sets of potential flow and boundary-layer solutions are used to obtain the final solution for the body. These three iterations have been found necessary to properly account for the coupling of the potential flow and a thick boundary layer on the body. This coupling is especially pronounced for a body on which the adverse pressure gradient takes the boundary layer to incipient separation. For example, in order to minimize drag, artillery projectiles are typically designed such that the conical boattail angle and length produce a boundary layer near separation, if not separated.

After each boundary-layer solution, the drag characteristics of the body are calculated. The toal drag of a body in incompressible flow is due to two sources: viscous shear and the pressure distribution. For these calculations, these two areas are further subdivided. The drag due to viscous shear is divided into three parts: that from the laminar boundary layer on the body C_{D_ℓ}, that from the turbulent boundary layer on the body C_{D_t}, and that due to the laminar and turbulent boundary layers on the aerodynamic surface $C_{D_{as}}$. The portion of drag due to pressure is subdivided into six components: drag due to the pressure on the base of the body C_{D_b}; drag due to the pressure on the base of the aerodynamic surfaces $C_{D_{asb}}$; drag due to pressure in the nonseparated flow portion of the body C_{D_p}; drag due to the pressure distribution in any separated region C_{D_s}; drag due to the pressure distribution about any attachment lugs $C_{D_{\rm lug}}$; and drag due to the pressure distribution about any firing band $C_{D_{\rm bnd}}$.

The boundary-layer solution and drag due to aerodynamic surfaces are calculated in the following manner. The surface planform is assumed to be trapezoidal with the tip chord parallel to the body axis. The points on the surface for the boundary-layer solution are determined by using a rectangular grid. Typically, each aerodynamic surface will have six grid points radially. Axially, grid points are determined by the spacing of the body surface points. The velocity at each of these grid points is calculated directly from the potential solution for the body. The pressure gradient at each grid point is calculated along the axial grid lines using only the axial velocity component. The boundary-layer solution is calculated along each axial grid line independently of the other axial grid lines. The skin friction drag exerted on the aerodynamic surface is calculated by integrating the shear stress distribution over the total surface area. The drag is converted to a drag coefficient, $C_{D_{as}}$, using the body reference area.

The present method has been implemented on a VAX 11/780 computer. Typical run times are on the order of 80 cpu seconds for a body with two sets of aerodynamic surfaces. The body is typically modeled with 30 source elements for the potential solution and 200 surface points for the boundary-layer solution. The computer time quoted includes three coupled potential/boundary-layer solutions with three sets of drag calculations.

Results

Pressure Distribution

Figure 3 compares the experimentally measured pressure coefficient[21] with the present method for a cone-cylinder-conical boattail body. This body was tested at a Reynolds number, based on length, of 7×10^6. Because this body was a quality wind tunnel model, a surface roughness of $k_s=1\times10^{-5}$ ft was used in the calculations. For this configuration, the boundary layer remained laminar until the nose-cylinder juncture. The strong adverse pressure gradient at that point caused boundary-layer transition. There was no separation on the boattail.

It can be seen that the agreement between theory and experiment is quite good. The maximum number of source elements which could be used in this calculation was 25. A greater number caused the surface streamline to undulate excessively between control points. As was noted by Christopher and Shaw,[6] the potential flow method used in the present work has difficulty in maintaining a constant body slope. In contrast to the behavior of the method for Rankine bodies, where increasing the number of source elements smoothed the body, bodies with constant slopes show greater streamline oscillations when

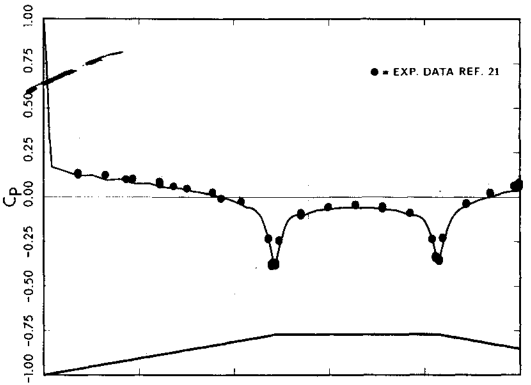

Fig. 3 Pressure distribution for cone-cylinder-boattail body.

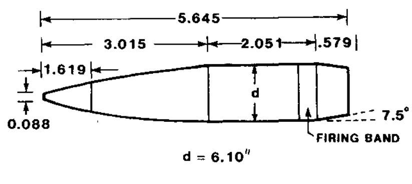

Fig. 4 M549A1/785 artillery projectile.

the number of source elements is increased. In extreme cases, the oscillations can become quite severe, rendering the potential solution meaningless.

A number of other comparisons between the present method and experiment have been made but will not be shown here. These comparisons were similar to those given in Refs. 4 and 7. The method gives good results for streamlined shapes which have a continuous variation of body slope over their length. Good results have been obtained for cone half-angles of 15 deg or less, but poor results were obtained for cone half-angles of 20 deg or higher. The only significant difference between the present results for pressure distribution and those of Ref. 4 is that the present method predicts peak pressure at points of surface discontinuity more accurately. As discussed earlier, this is due to the improved location of the body surface control points in the potential flow solution.

Drag Predictions

In order to make accurate calculations of the drag of a body, one must have an accurate estimate of the surface roughness. Table 3 shows a compilation of equivalent sand-grain roughness values for a variety of common surfaces (from Refs. 10 and 22). In determining the values of roughness used for the drag comparisons in this report, an effort was made to correlate the character of the different surfaces from Table 3 with the actual surface of the body in question. There are several difficulties, however, in attempting to estimate the surface roughness. First is the nature of the effect of surface roughness on drag. Schlichting[12] gives a good description of surface roughness effects on skin-friction drag. He points out that skin-friction drag depends upon the density distribution of the roughness elements, the shape, the height, and the manner in which they are distributed over the surface. Therefore, roughnesses of particular surfaces are given in terms of an equivalent roughness of uniform sand-grain roughness k_s. For certain types of roughness, e.g., rivet heads, he gives a table of their equivalent sand-grain roughness.

Table 3 Values of equivalent sand grain roughness for typical surfaces

Type of surface	k_s, ft	Ref.
High quality glass	1×10^{-6}	10
Metal or wood, highly polished	2×10^{-6}	10
Metal or wood, polished	7×10^{-6}	10
Drawn tubing	5×10^{-6}	10
Natural sheet metal	13×10^{-6}	22
Smooth matte paint, carefully applied	21×10^{-6}	22
Camouflage paint, average application	33×10^{-6}	22
Camouflage paint, poor application	100×10^{-6}	22
Steel, wrought iron	150×10^{-6}	10
Asphalted cast iron	400×10^{-6}	10
Dip galvanized metal, new	500×10^{-6}	10
Dip galvanized metal, old	900×10^{-6}	10
Natural cast iron	830×10^{-6}	22
Concrete, excellent finish	1×10^{-3}	10
Concrete, poor finish	1×10^{-2}	10

The equivalent sand-grain roughness is the average diameter of the sand grains. When specifying a surface finish of metal, this approximately corresponds to the average peak to valley height of the actual surface roughness. The standard specification given on engineering drawings, however, is the average surface roughness. This average surface roughness is approximately one-fourth of the average peak to valley roughness according to General Electric Standard Roughness Specimens.

The second, and more important, problem in correlating the actual surface roughness to an equivalent sand-grain roughness is the lack of documentation on surface quality. None of the reports describing the acquisition of the drag data used to verify the theory give a precise, quantitative description of the surface finish. Neither do they give a detailed description or photographic documentation of vehicle joints or fasteners. Faced with this dilemma, a careful effort was made to estimate consistently the surface roughness on all of the bodies based on the equivalent sand-grain roughnesses given in Table 3.

Table 4 contains drag predictions from the present method and drag measurements from a number of experiments.[23-29] In selecting these experimental data for comparison, only free-flight data were used, except for the two missile configurations in the Table. For the missile configurations, wind tunnel data were used with the base drag removed from the measurements. That is, for the missile configurations, the drag quoted for both the present method and the experiment assumes $C_{D_b} = 0$.

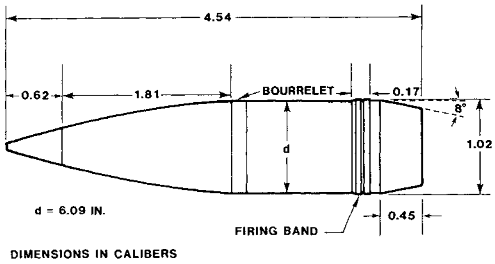

Fig. 5 M107 artillery projectile.

Table 4 Comparison of drag predictions with test data[a]

Body	C_{D_ℓ}	C_{D_t}	C_{D_p}	C_{D_b}	C_{D_s}	$C_{D_{\text{bnd}}}$	$C_{D_{\text{lug}}}$	$C_{D_{\text{as}}}$	$C_{D_{\text{as}_b}}$	$C_{D_{\text{theory}}}$	$C_{D_{\text{exp}}}$	$\dfrac{C_{D_{\text{theory}}}}{C_{D_{\text{exp}}}}$	Re_L, $\times10^{-6}$	Ref.
M549/785	0.0003 (<1)	0.0829 (66)	0.0154 (12)	0.0247 (20)	0	0.0023 (2)	0	0	0	0.126	0.118	1.07	9	23
M107	0.0012 (1)	0.0613 (55)	0.0172 (16)	0.0272 (24)	0.0022 (2)	0.0024 (2)	0	0	0	0.112	0.123	0.91	7	24
AEDC cone	0.0058 (2)	0	−0.0055 (−2)	0.2979 (100)	0	0	0	0	0	0.298	0.300	0.99	2	25
NASA flare	0.0013 (<1)	0.0111 (3)	0.0721 (16)	0.3657 (81)	0	0	0	0	0	0.450	0.460	0.98	8	26
B83	0.0026 (1)	0.0686 (28)	−0.0062 (−3)	0.1300 (53)	0 0	0 0	0.0299 (12)	0.0074 (3)	0.0142 (6)	0.246	0.250	0.98	39	27
B61	0.0037 (2)	0.0795 (41)	0.0593 (31)	0	−0.0089 (−5)		0.0337 (17)	0.0186 (10)	0.0067 (4)	0.192	0.190	1.01	38	28
Missile 1	0.0067 (2)	0.1467 (36)	0.0103 (3)	0	0	0	0	0.2373 (59)	0	0.401	0.400	1.00	11	29
Missile 2	0.0067 (2)	0.1467 (37)	0.0103 (3)	0	0	0	0	0.2300 (58)	0	0.394	0.400	0.99	11	29

[a] Numbers in parentheses = % of predicted drag.

In Table 4, all of the drag components due to pressure are referenced to the freestream static pressure, i.e., if a pressure drag component is zero, then the integrated average of the pressure producing that drag is equal to P_∞.

The first two entries in Table 4 are for artillery shells, M549A1/785 and M107. The external geometries of these shapes are shown in Figs. 4 and 5. These shapes have secant ogive noses, cylindrical midsections, and conical boattails. For the potential solution, these bodies were modeled with 30 source elements. The experimental data for these shapes were taken from free-flight tests of production type rounds, not from smooth wind tunnel models. The surfaces of these rounds are characterized by nose fuse slots, mismatch of the diameters of the threaded sections, and by chipped and scratched paint. The surface conditions are, therefore, relatively rough and ill-defined. A value of $k_s = 3 \times 10^{-4}$ ft was chosen to model these bodies. In both cases, the roughness was sufficient to cause the boundary layer to transition early on the nose.

As shown in the table, the drag predictions are within 10% of the experimental measurements for both of these artillery projectiles. In each case, the major component of drag is due to turbulent skin friction. These values range from 55% for the M107 to 66% for the M549. The base drag component varies from a low of 20% for the M549 to 24% for the M107. On these artillery projectiles, the firing-band drag contribution is 2%. For supersonic speeds, however, the firing-band contribution increases significantly due to wave drag. Flow separation was predicted on the boattail of the M107 shape. The drag contribution of the pressure within the separated region was 2%. Although the boundary layer remained attached on the M549, the shape factor H was just below the separation criterion, indicating that the boundary layer was just barely attached. The shape factor on the M107 grew slowly until near the midpoint of the boattail length and then it exceeded the separation criterion.

The third entry in Table 4 is for a 10 deg half-angle cone called AEDC cone. The body geometry is shown in Fig. 6. This body was modeled with 20 source elements. Because it was a ballistic range free-flight model with good surface quality, the surface was considered to be natural sheet metal and $k_s = 1 \times 10^{-5}$ ft. This shape was predicted to have a laminar boundary layer over the entire body length. The predicted drag coefficient is within 1% of the test value. To those unfamiliar with drag of cones at subsonic speeds, it is surprising that all of the drag is due to base drag. The skin-friction drag is offset by the negative contribution of the surface-pressure drag. Because of the good agreement with experimental measurements and the high percentage of base drag of this and other conic bodies, the accuracy of the base pressure estimate for conical bodies is confirmed.

The next table entry, designated NASA flare and shown in Fig. 7, has a tangent ogive nose, a cylindrical midsection, and a 20 deg conical flare. It was modeled with 15 source elements and was assumed to have a surface roughness of natural sheet metal, $k_s = 1 \times 10^{-5}$ ft. The predicted drag is within 2% of the experimental value. As with the cone, the majority of the drag, 81%, is due to base drag. For this body, the boundary layer was calculated to transition at the nose-cylinder juncture. The presence of the large adverse pressure gradient just ahead of the cylinder-flare juncture caused the boundary layer to separate and reattach on the flare.

The next two entries in Table 4 are for bomb shapes. As these bombs typically have a quality painted finish and few joints and surface irregularities, a value of $k_{sa} = 30 \times 10^{-6}$ ft was used in the calculations. Both bodies were modeled with 30 source elements. On both bodies, boundary-layer transition occurred just aft of the nose-cylinder juncture. On the fins, transition occurred approximately 10 in. aft of the fin leading edge. The experimental drag coefficients were determined from a large number of free-flight drop tests. When examining the drag components of these bombs, it is informative to contrast the differences in pressure drag components between the two bomb shapes. Such a contrast shows the tradeoffs which are made when one tries to reduce drag through boattailing.

The first bomb shape is the B83 shown in Fig. 8. This body is a secant ogive-cylinder. The drag prediction on this bomb shape is within 2% of the experimental value. For this body, over half of the drag, 53%, is due to the base pressure. This high value occurs because the body does not have any boattail. Because the body has a zero body slope over most of its length, the drag contribution of the pressure distribution is negative, −3%. The high pressure near the nose tip is overcome by the low (less than P_∞) pressure near the ogive-cylinder juncture yielding negative drag. The other large drag component, 28%, is body skin friction. The two attachment lugs contributed 12% and the fins accounted for 9% of the drag; 3% due to skin friction, and 6% due to fin base pressure.

The second bomb entry is the B61, shown in Fig. 9. The B61 has a streamlined nose followed by a cylindrical midsection

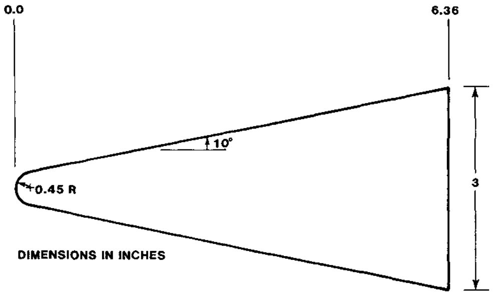

Fig. 6 AEDC cone.

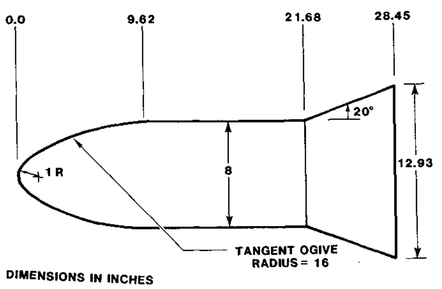

Fig. 7 NASA flare.

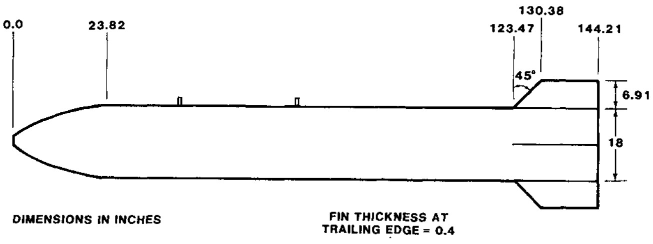

Fig. 8 B83 bomb.

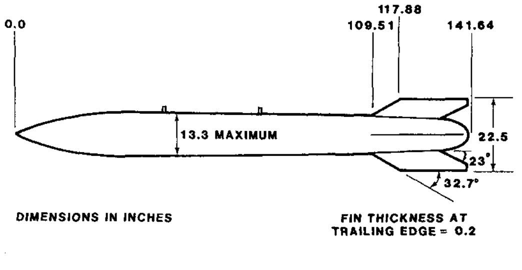

Fig. 9 B61 bomb.

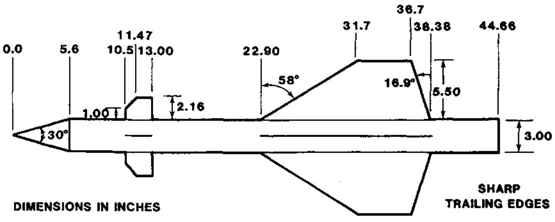

Fig. 10 Missile 1 with canard control.

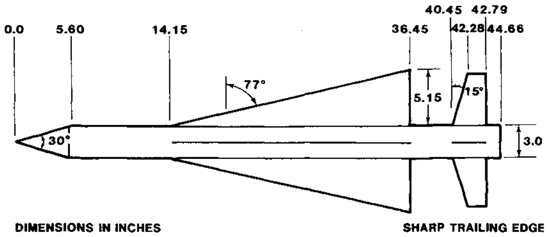

Fig. 11 Missile 2 with tail control.

from 22 to 56% of length. The boattail is parabolic with a spherical tail cap. On the body, separation occurs at 99% of length. The drag estimate on this bomb is within 1% of the experimental value. About half of the drag, 41%, is due to laminar and turbulent skin friction on the body. Because the body has a spherical tail cap, it was modeled as a closed body. Therefore, by the present definition, there is no base drag. The B61 aft contour allows the pressure to recover above freestream static pressure before separation occurs. The pressure drag in the attached flow region was 31% and within the separated region it is estimated to be −5%. The drag on the two lugs accounted for a surprising 17% of the drag and the fins accounted for 14%. As an independent check on the lug drag, the lug drag given in the table was compared with wind-tunnel data on the B61. The wind-tunnel experiment determined that the lug drag component was 0.033, which is essentially identical to the prediction in Table 4.

The last two entries in Table 4 are for missile shapes shown in Figs. 10 and 11. Both of these bodies have the same conical nose and cylindrical body and were modeled with 30 source segments. The differences occur in the type and shape of the aerodynamic surfaces. Missile 1, Fig. 10, has a large wing and small canards for control. Missile 2, Fig. 11, has a highly swept wing with large control fins. These bodies were wind-tunnel models tested with a sting mount. The wind-tunnel base drag was subtracted from the experimental measurements. Therefore, neither the calculated nor experimenal drag values shown in Table 4 include base drag. The bodies were high quality wind-tunnel models, thus a surface roughness of $k_s = 1 \times 10^{-5}$ ft was used in the calculations. Boundary-layer trip strips were placed on the model approximately 3 cm aft on the nose and 1.02 cm aft of the wing and canard/tail leading edges. In the theory, therefore, the boundary layers on the aerodynamic surfaces were forced to transition at the locations of the trip strips.

Table 4 shows that the drag predictions for both configurations are within 1% of the experimental measurement. For both configurations, the major drag contributor, 58%, is due to the aerodynamic surfaces. This quantitatively illustrates the drag penalty one must pay if high maneuverability is desired. The wings on these bodies had sharp trailing edges so there was no fin base drag. On the body, the major drag contributor was skin friction. If base drag had been included, the drag of Missile 1 and Missile 2 would have been 0.531 and 0.524, respectively.

Conclusions

A design method is presented which provides the designer with accurate predictions of the flowfield and drag components of bodies of revolution, with and without aerodynamic surfaces, at zero angle of attack in incompressible flow. A number of comparisons between the present method and experimental measurements of surface pressure distributions have been made. The present method gives good results for streamlined shapes and geometries without a blunt nose. Good results were obtained for cones and cone-cylinders with cone half-angles of 15 deg or less, but poor results were obtained for cone half-angles of 20 deg or greater. For large cone angles, it was found that the computed surface streamline tends to undulate between the body control points degrading the solution.

Comparisons between drag prediction and measurement were good for a wide variety of vehicle geometries. For production artillery shells, the drag predictions were shown to be accurate to within ±10%. The drag predictions for cones and flared bodies were shown to be accurate to within ±2%. For fin-stabilized bomb shapes and missiles with large wings, the method was shown to be accurate to within ±1%. Based on these comparisons, and many others not presented here, the accuracy of the predicted drag coefficients should be conservatively within ±10% for freestream Mach numbers less than the critical Mach number of the geometry.

The computer code SANDRAG is easy to use and requires only simple inputs. Extensive testing and verification of the code has been conducted. The breakdown of the total drag into its various components allows the designer to ascertain quantitatively all of the drag contributors. This information can then aid the designer in directing efforts toward those areas where the potential for drag reduction is greatest. This method can also be used for parametric investigation of the effects of geometric changes on the flowfield and drag.

Acknowledgments

This work was performed at Sandia National Laboratories and was supported by the U.S. Department of Energy under Contract DE-AC04-76DP00789.

References

[1]Hess, J.L. and Smith, A.M.O., "Calculation of Potential Flow About Arbitrary Bodies," *Progress in Aeronautical Sciences,* Vol 8, Pergamon Press, New York, 1967, pp. 1-138.

[2]Oberkampf, W.L. and Watson, L.E., "Incompressible Potential Flow Solutions for Arbitrary Bodies of Revolution," *AIAA Journal,* Vol. 12, March 1974, pp. 409-411.

[3]Zedan, M.F. and Dalton, C., "Potential Flow Around Axisymmetric Bodies: Direct and Inverse Problems," *AIAA Journal,* Vol. 16, March 1978, pp. 242-250.

[4]Wolfe, W.P. and Oberkampf, W.L., "A Design Method for the Flow Field and Drag of Bodies of Revolution in Incompresible Flow," AIAA Paper 82-1359, Aug. 1982.

[5]Zedan, M.F. and Dalton, C., "Higher-Order Axial Singularity Distribution for Potential Flow about Bodies of Revolution," *Computer Methods in Applied Mechanics and Engineering,* Vol. 21, 1980, pp. 295-314.

[6]Christopher, P.A.T. and Shaw, C.T., "Generation of Axisymmetric Body Shapes in Subsonic Flow by Means of Polynomal Distributions of Source and Doublets Along the Axis of Symmetry," Cranfield College of Aeronautics, Memo 8110, Cranfield, England, Oct. 1981.

[7]Wolfe, W.P. and Oberkampf, W.L., "SANDRAG—A Computer Code for Predicting Drag of Bodies of Revolution at Zero Angle of Attack in Incompressible Flow," Sandia National Laboratories, Albuquerque, NM, SAND85-0515, April 1985.

[8]Wolfe, W.P. and Oberkampf W.L., "SANDRAG—A Computer Code for Predicting Drag at Zero Angle of Attack in Incompressible Flow," Sandia National Laboratories, Albuquerque, NM (in preparation), 1987.

[9]Thwaites, B., "Approximate Calculation of the Laminar Boundary Layer," *Aeronautical Quarterly,* Vol. 1, Nov. 1949, pp. 245-280.

[10]White, F.M., *Viscous Fluid Flow,* McGraw-Hill, New York, 1974, pp. 241-558.

[11] Casarella, M.J. and Niedzweicki, J.M., "Predicting the Effects of Surface Roughness on Laminar-Turbulent Transition for Axisymmetric Bodies," *Journal of Hydronautics*, Vol. 14, July 1980, pp. 83-90.

[12] Schlichting, H., *Boundary-Layer Theory*, 6th ed., McGraw-Hill, New York, 1968, pp. 431-651.

[13] Kluck, C.E., "Prediction of Laminar-to-Turbulent Boundary Layer Transition in Axial-Flow Turbomachinery," Air Force Office of Scientific Research, AFOSR-TR-81-0806, Dec. 1981.

[14] Sovran, G., "On Prediction Criteria for Turbulent Separation," *Proceedings: Computation of Turbulent Boundary Layers—1968 AFOSR-IFP Stanford Conference*, Vol. 1, Stanford University, Stanford, CA, 1969, pp. 447-450.

[15] White, F.M., "A New Integral Method for Analyzing the Turbulent Boundary Layer With Arbitrary Pressure Gradient," *Journal of Basic Engineering*, Sept. 1969, pp. 371-376.

[16] McCoy, R.L., "MC DRAG—A Computer Program for Estimating the Drag Coefficients of Projectiles," Ballistic Research Laboratory, Aberdeen Proving Ground, MD, ARBRL-TR-02293, Feb. 1981.

[17] Payne, P.R., Hartley, R.M., and Taylor, R.M., "Afterbody Drag, Volume 1—Drag of Conical and Circular Arc Afterbodies Without Jet Flow," David W. Taylor Naval Ship R&D Center, Bethesda, MD, DTNSRDC/ASED-80/10, May 1980.

[18] Pepper, W.B. and Holland, T.R., "Transonic Pressure Measurements on Blunt Cones," Sandia Corporation, Albuquerque, NM, SC-4157 (TR), May 1958.

[19] Butsko, J.E., Carter, W.V., and Herman, W., "Development of Subsonic Base Pressure Prediction Methods," Air Force Flight Dynamics Laboratory, Wright-Patterson Air Force Base, OH, AFFDL-TR-65-157, Vol. 1, Aug. 1965.

[20] Engineering Design Handbook: "Design of Aerodynamically Stabilized Free Rockets," U.S. Army Material Command, AMCP-706-280, July 1968 (AD840582), p. 867.

[21] Fox, C.H., Jr., "Experimental Surface Pressure Distributions for a Family of Axisymmetric Bodies at Subsonic Speeds," NASA TM X-2439, Dec. 1971.

[22] *USAF Stability and Control DATCOM,* McDonnell Douglas Corp., Air Force Flight Dynamics Laboratory, Wright-Patterson Air Force Base, OH, Oct. 1960 (revised Jan. 1975).

[23] Whyte, R.H., Burnett, J.R., Hathaway, W.H., and Brown, E.F., "Analysis of Free-Flight Aerodynamic Range Data for the 155-mm M549 Projectile," US Army Armament Research and Development Command, Dover, NJ, ARLCD-CR-80023, Oct. 1980.

[24] MacAllister, L.C. and Krial, K.S., "Aerodynamic Properties and Stability Behavior of the 155mm Howitzer Shell, M107," Ballistic Research Laboratories, Aberdeen Proving Ground, MD, Memorandum Rept. 2547, Oct. 1975.

[25] Starr, R.F. and Watt, R.M., "Free-Flight Range Tests of Blunted Bodies of Revolution at Transonic Speeds," Arnold Engineering Development Center, Arnold Air Force Station, TN, AEDC-DR-75-77, Aug. 1975.

[26] Coltrane, L.C., "Stability Investigation of a Blunted Cone and a Blunted Ogive with a Flared Cylinder Afterbody at Mach Numbers From 0.30 to 2.85," NASA TMX-199, Nov. 1959.

[27] Everett, R.N., "Aeroballistic Performance of the B83 Bomb in the Freefall Delivery Mode," Sandia National Laboratories, Albuquerque, NM, SANDS83-8221, July 1984.

[28] Wheat, G.S., "Exterior Ballistic Analysis of Nuclear Bomb B61/Unretarded (U)," Naval Weapons Laboratory, NWL TR-2690, Jan. 1972 (CONF).

[29] Corlett, W.A. and Howel, D.T., "Aerodynamic Characteristics at Mach 0.60 to 4.63 of Two Cruciform Missile Models, One Having Trapezoidal Wings with Canard Controls and the Other Having Delta Wings with Tail Controls," NASA-TM-X-2780, July 1973.